Wireless and Zero-Power Trans-Cardiac Link With Antennified Aortic Valve Bioprostheses

Federica Naccarata ⓘ, *Graduate Student Member, IEEE*, Cecilia Occhiuzzi ⓘ, *Member, IEEE*, Roberto Verzicco, and Gaetano Marrocco ⓘ, *Senior Member, IEEE*

Abstract—**Valvular heart diseases are one of the most common complications in the cardiovascular system. To restore the correct cardiac activity, the failing native heart valve is surgically replaced with a prosthesis. Unfortunately, it often undergoes physio-pathological processes after implantation, including the risks of functional and structural deterioration. Periodic monitoring is hence mandatory all along the life of the patient. As standard screenings are intrusive, this paper proposes a method to exploit the peculiar form-factor of the internal metallic stent of a bioprosthesis as a natural energy harvester to achieve a reliable wireless trans-cardiac RFID-based, battery-free, communication link with no relevant change to the valve. Simulations and tests with a mock-up demonstrate that a robust link with a small size on-skin patch antenna is feasible notwithstanding potential user-specific placement as well as misalignment between the antennas.**

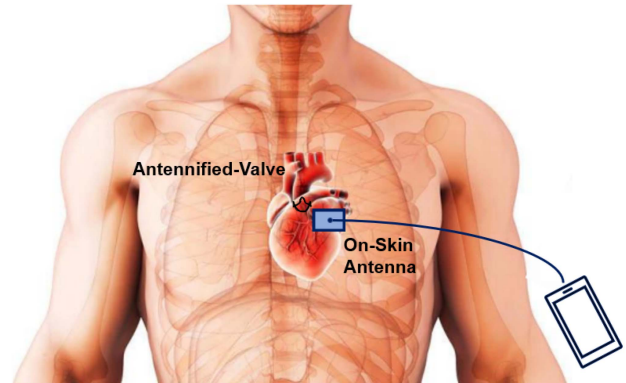*Index Terms*—**Implantable antenna, radio frequency identification (RFID), cyber-prosthesis, wireless monitoring.**

Fig. 1. Concept of a remote interrogation of an RFID-based antennified-prosthesis to evaluate the local biophysical parameter.

I. INTRODUCTION

WITH an incidence of about 25%, heart disease is the first cause of death in the US [1]. Among the different causes, valvular heart injuries such as stenosis, insufficiency, and regurgitation are the most common forms of complications affecting more than 100 million people worldwide, with significant mortality and morbidity [2]. Generally, to restore the correct cardiac activity and prevent heart failure, the damaged native heart valve is surgically replaced with a prosthesis [3], that is capable to force the unidirectional flow of the blood and hence restore the transvalvular pressure gradients [4].

Unfortunately, valve prostheses often undergo pathophysiological processes, including the risks of thromboembolism, infection, prosthetic endocarditis, and structural deterioration [5]. Periodic monitoring of the valve status and operation is hence mandatory all along the life of the implant. Standard screenings involve electrocardiogram, phonocardiogram signal analysis, transesophageal echocardiography, multidetector computed tomography, cardiac magnetic resonance imaging, and cinefluoroscopy [6], [7]. These tests, however, are time-consuming, intrusive, and with a long turnover for the patient.

New tools currently under study, and experimentation for clinical prevention, diagnosis, and treatment [8] include implanted medical prostheses with embedded sensors and wireless communication. In an envisaged diagnostic scenario, a clinician will place a small-size transmitter antenna on the patient's thorax to interrogate the implanted sensorized heart valve prosthesis and obtain data that can be processed to tune personalized treatments [9] (Fig. 1). In addition, this could be an enabling tool to feed a Digital Twin of the patient that continually adapts the digital representation based on the collected data over time [10].

In recent years, some cardiovascular implanted devices have been already equipped with sensing and data transmission capabilities, as in the case of CardioMEMS [11], the V-LAP system [12], implantable loop recorders, leadless pacemakers, and subcutaneous cardioverter-defibrillators [13]. The detection of reduced motility of the prosthesis leaflets, due to thrombus formation, through an electric impedance measurement is described in [2]. A nitinol active stent for non-invasive restenosis treatments using a radiofrequency (RF) electro-thermo-mechanical technique for wireless revascularization is proposed in [14]. Moreover, an implantable blood flow sensor attached to the ascending aorta can be found in [3].

However, the above examples of wireless telemetry do not concern heart valve prostheses. Furthermore, most of these devices are bulky and highly invasive, namely, they are intrusive objects that in some cases require a battery that takes a significant volume and needs to be replaced after a while.

We propose here a different approach, aiming at simplifying the architecture of a battery-less wireless valve prosthesis,

that minimizes the amount of additional electromagnetic and electronic components to limit the structural modifications of the valve and hence not hinder its mechanical activity and the fluid dynamics of the blood [15]. For this purpose, the internal metallic stent of the valve will be exploited as a natural energy harvester at the frequency of 900 MHz. With respect to other possible options (HF 13.56 MHz, MedRadio 403 MHz, ISM microwave 2.45 GHz), the selected frequency is the only one capable to enable a reasonable penetration depth and a battery-less data exchange by means of the Radio Frequency Identification (RFID) technology in the UHF (860–960 MHz) band.

The concept of transforming a structural metal object into an antenna (*antennification*), as in [16], has been already considered for some implantable medical devices and mainly refers to the dipole-like radiating mode. For instance, the helicoidal steel wires of an implanted stent for abdominal aortic aneurysm was augmented in [17] with a feeding copper wire connected to the upper and lower mid-portion of the stent to achieve a Γ-match dipole excitation. The resulting modification of the medical device is however not negligible since the rigid interconnection makes the stent stiffer. A similar strategy, still involving an additional rigid wire and the same drawback, was exploited in [18] to provide a stent with an RFID IC with the purpose to detect re-stenosis. A stent, was also integrated with a capacitive pressure sensor in [14], [19] to work as a resonant circuit and communicate with an external coil through a resonant inductive coupling. Moving to the orthopedic field, a metallic bone-plane fixture in [20] was transformed into a flat energy harvesting dipole by the insertion of a plug-and-play disk adapter into unused screw holes. Finally, an antennified dental implant is described in [21], where a small PCB disk is integrated into the crown to excite the abutment, and achieve an asymmetric dipole. The above methods can not be applied to closed-loop wireframes, like the stent of the aortic valve, since they can not be either interrupted to add electronics, or soldered to additional wires, and therefore a different antennification must be investigated. For this purpose, by expanding the preliminary work in [22], this paper proposes to provide the meandered stent of the valve with a tiny loop harvester, electromagnetically coupled to it, that does not require any electrical or mechanical interconnection. Nevertheless, it is capable to take advantage of the valve as the main radiator activating a loop-like radiating mode suitable to communicate via UHF backscattering modulation. The goal is to achieve a reliable trans-cardiac battery-free (zero-power) link with an interrogating antenna placed on the thorax, notwithstanding the implantation depth of 7 cm within a highly lossy environment.

The paper is organized as follows. The rationale of the idea and the models of the aortic valve prosthesis and human thorax are introduced in Section II. Section III describes the electromagnetic modules to be optimized and the network model to account for the mid-field link between the valve and the interrogator. Section IV resumes the numerical simulations for the optimization of the loop harvester, also evaluating the communication
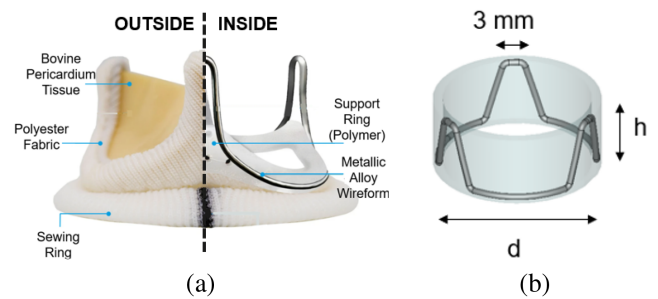

Fig. 2. (a) Example of a biological aortic valve prosthesis, (adapted from model Dafodil by Meril Life [23]), where the Co-Cr-Ni alloy stent is encapsulated by white polyester fabric. (b) Simplified CAD model of the metallic stent with the dielectric coating ($h = 9.5$ mm; $d = 24$ mm; wire diameter 1 mm).

robustness versus possible misalignment and the safety constraints related to exposure limits. Finally, Section V summarizes some preliminary experimental tests with a mock-up of the device, demonstrating, in-vitro, the feasibility of the proposed trans-cardiac link.

II. RATIONALE AND MODELS

A. Aortic Valve Layout

Two types of valve prostheses are generally used: mechanical and biological. Mechanical valves comprise fully engineered objects which are fabricated in titanium and pyrolitic carbon (balls, tilting discs, leaves) [24]. Biological valves, instead, consist of semi-lunar-shaped leaflets of animal origin (bovine, porcine, or human tissues). The leaflets are properly mounted on a supporting structure, namely a stent, with its cusps [25]. Currently, the stents are composed of metallic alloys or polymers. The stent is attached to a basal circular ring, which is normally made of silicone rubber or polyester coated by a fabric sewing cuff, that facilitates suturing to the native aortic annulus. We will focus, hereafter, on biological valves with a metallic stent, such as that in Fig. 2(a). Without any loss of generality, all the simulations reported next will be accordingly referred to the simplified model (Fig. 2(b)) comprising the metallic stent and the external dielectric coating, that acts also as a holding structure (polyester $\varepsilon = 2.1$, $\tan \delta = 0.0035$ [26]).

Similarly, the portion of the human thorax is emulated by an anthropomorphic thorax model of layered (skin, fat, muscle) elliptical cylinder including the ribcage, sternum, and lungs [22] (Fig. 3). The valve is inserted in the aorta at the depth of 7 cm from the skin. As a conservative electromagnetic case, the heart and the aortic vessel are considered always filled with blood. The electrical parameters of the tissues at 900 MHz are listed in Table I.

B. Stent as Meandered-Loop Antenna

The metallic stent (simulated as steel $\sigma = 7.69 \times 10^6$ S/m) inside the valve prosthesis can be considered as a shaped loop
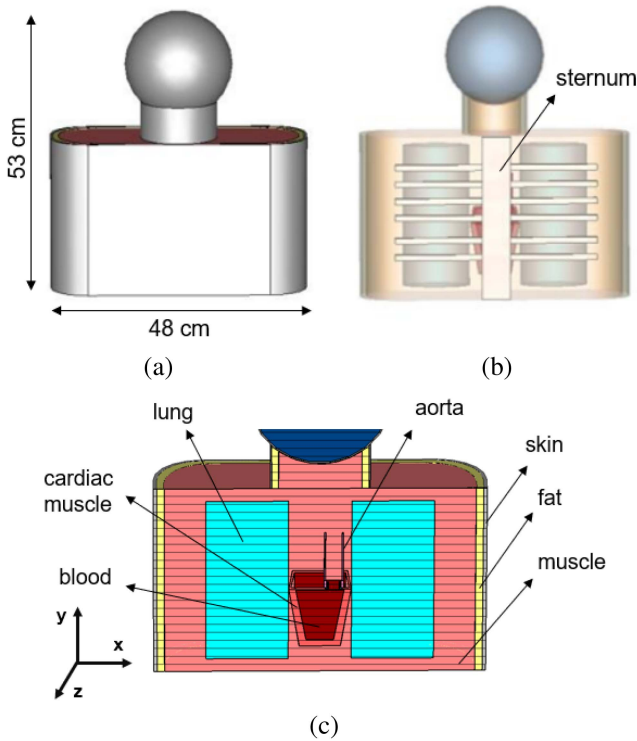
(a)

(b)

Fig. 3. Reference model of the thorax for electromagnetic simulations: (a) sizes, (b) internal structures, and (c) cutting view [22].

(c)

TABLE I
ELECTRICAL PROPERTIES OF THE TISSUES AT 900 MHz [27]

	$\sigma[\frac{S}{m}]$	ε_r
Aorta	0.70	44.78
Blood	1.54	61.36
Bone	0.14	12.90
Cardiac Muscle	1.23	59.89
Fat	0.05	05.46
Lung	0.46	22.00
Muscle	0.94	55.00
Skin	0.86	41.40

with the three cusps acting as meanders. To analyze the performance of the device as an antenna, the current pattern that it can sustain at 900 MHz is preliminarily evaluated by exciting it in the center of a cusp by a voltage gap. All electromagnetic simulations are performed by using the Finite Element Method in CST Microwave Studio 2018. The obtained surface current (Fig. 4) resembles that of a typical λ-loop [28]. As nulls are located in the middle of the stent, the two half portions of the structure host in-phase currents. The radiated electric field on the thorax surface has mostly horizontal components in front of the prosthesis (Fig. 5) that can be coupled with a linearly polarized on-skin antenna. By reciprocity, the metal stent of the valve can be hence considered a natural energy harvester at 900 MHz.

III. ENERGY HARVESTING

The *Antennification* of the stent inside the valve, requires to define a minimal conformable add-on to convey the energy harvested by the metallic stent, during the exposure to an external
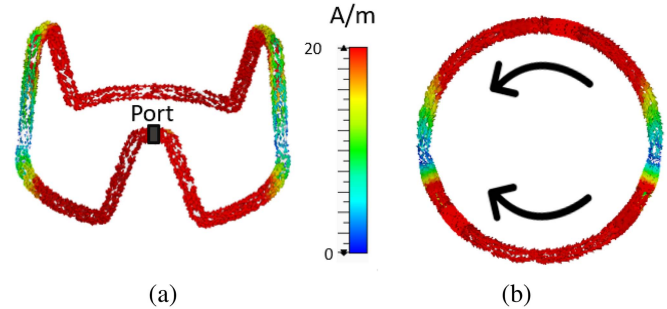

Fig. 4. Simulated surface currents at 900 MHz onto the valve metal stent when it is excited in the middle of a cusp by a voltage gap: (a) frontal view, and (b) top view.
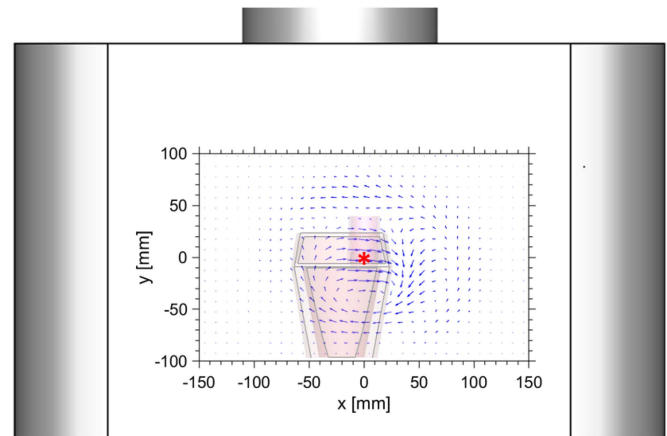

Fig. 5. Simulated normalized electric field over a portion of the surface of the thorax. The red star identifies the footprint of the stent.

interrogator, toward the transponder electronics, namely the RFID-IC. This goal is accomplished by coupling a cusp of the stent with a trapezoidal loop, hence leaving the aortic lumen unaffected. The coupler is embedded into the same dielectric coating of the stent to preserve the structural stability of the valve and thus its mechanical and fluid-dynamic performance. This approach does not require interrupting the stent to insert the feeding, and accordingly, the structure of the prosthesis is left intact.

A. Trapezoidal Coupled Loop

For the sake of modeling, and above all of the manufacturing simplicity, the trapezoidal loop is assumed made of a planar copper trace (width = 1 mm, thickness 0.035 mm) laying on a Kapton film (thickness 0.125 mm, $\varepsilon = 3.5$, $\tan\delta = 0.0026$ [29]), (Fig. 6), and insulated by the same dielectric coating of polyester of the stent to avoid the direct interaction with the body fluids. The Kapton, that is a flexible but not stretchable substrate, allows following the curvilinear profile of the cusp without a bulky thickening. However, it is not suitable to preserve the natural elasticity of the cusp, even though there is no rigid connection with the stent. For a real application, instead, the electronic circuitry could be directly transferred by inkjet or transfer printing [30] on a ultra-thin elastomeric film, having Young's modulus comparable to that of the aortic wall (840 kPa [31]),
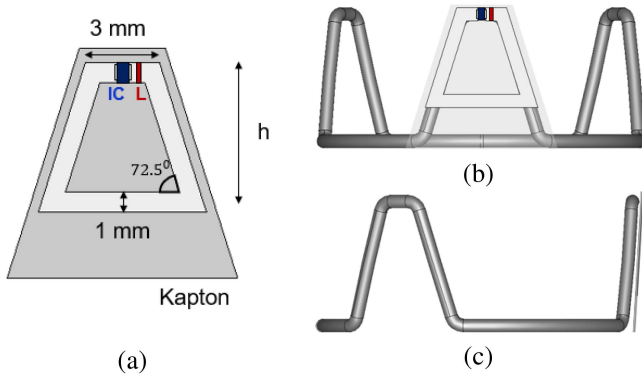
Fig. 6. Trapezoidal loop-match to couple the RFID IC to the stent of the valve: (a) loop sizes and location of the IC and inductor for impedance matching, (b) front view, and (c) lateral view.

like polydimethylsiloxane (1.8 MPa [32]) or polyurethane (1.2 MPa [33]).

The length of the shorter base and the angles of the trapezoidal loop are considered fixed to follow the profile of the cusp. The height of the loop (h) and a series inductor (L), close to the port, are the free parameters to be optimized to maximize energy harvesting.

B. Self-Tuning ICs

The reference IC, for simulations and experimentation, is the Magnus-S3 by Axzon with power sensitivity, i.e. the minimum output power from the reader delivered to the IC so that it wakes up and starts operating, equal to $P_{chip} = -13.6$ dBm and equivalent input impedance $Z_{chip} = 2.6 - j73.6 \ \Omega$ at 900 MHz [34]. It is an example of a sensor-oriented IC since it is provided with an embedded temperature sensor and can be also interfaced with external potentiometric [35] and amperometric sensors [36]. The IC exploits a self-tuning feature that permits to modify its internal radiofrequency susceptance (around the above nominal value) to compensate for possible mismatching with the antenna and to maximize the power delivered to the IC. The architecture of the IC can be modeled as a resistor in parallel with an adaptive internal switched network of a ladder of capacitors, with overall capacitance C_{IC} [37]:

$$C_{IC}(s) = C_{\min} + sC_{\text{step}} \tag{1}$$

where $C_{\min} = 1.9$ pF is the baseline, $C_{\text{step}} = 3.1$ fF is the incremental step and $s \in \{s_{\min} = 80, \ s_{\max} = 400\}$. Accordingly, the equivalent susceptance $B_{IC}(s) = 2\pi f C_{IC}(s)$ automatically adapts to satisfy the matching condition:

$$|B_{IC}(s) + B_A| = 0 \tag{2}$$

where f is the frequency and B_A the antenna's susceptance.

C. Reader Antenna

The considered reader antenna is a linearly polarized microstrip slot as in [38] (layout in Fig. 7(a)) placed on the patient's chest at heart level (Fig. 7(b)) and oriented to couple with
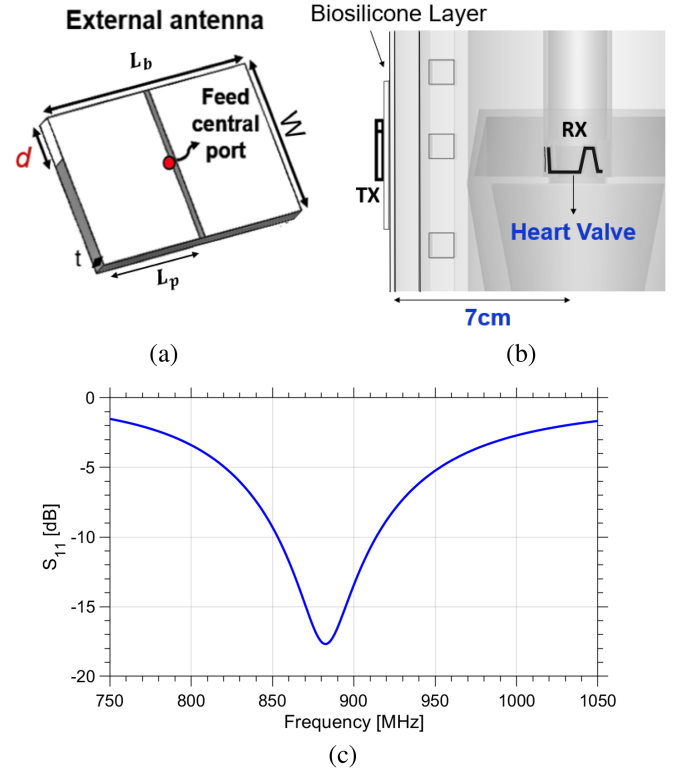

Fig. 7. On-skin reader's microstrip antenna, from [38], involved in the evaluation of the trans-cardiac link: (a) layout of the microstrip slot antenna ($L_b = 40$ mm, $W = 25$ mm, $L_p = 19.5$ mm, $d = 2$ mm and $t = 3$ mm) and (b) arrangement on the anthropomorphic thorax through a 2 mm silicone layer. (c) Simulated reflection coefficient of the optimized reader antenna.

the dominant component of the electric field of the stent. It is assumed to be put in touch with the skin by means of a silicone layer (thickness 2 mm, $\varepsilon = 2.2$, $\sigma = 0.005$ S/m [39]).

D. Two-Port Link

The through-the-body link between the interrogating on-thorax antenna and the antennified valve is here modeled [40] by a lossy two-ports network that is characterized through its impedance matrix: port 1 (input) and port 2 (output) are the reader' s antenna and the implanted device terminals, respectively. This model is able to capture the whole near-field interactions, where both electrical and magnetic phenomena are involved. The communication performance is quantified by the Transducer Power Gain (G_T), i.e. the ratio between the power delivered by the reader to the IC $P_{R \to T}$ and the available power of the generator $P_{av,R}$. G_T can be expressed in terms of admittance [41]

$$G_T = \frac{P_{R \to T}}{P_{av,R}} = \frac{4G_g G_{IC} |Y_{12}|^2}{|(Y_{11} + Y_g)(Y_{22} + Y_{IC}) - Y_{12}^2|^2} \tag{3}$$

where $Y_g = G_g + jB_g$ and $Y_{IC} = G_{IC} + jB_{IC}$ are the internal admittance of the reader and the IC's admittance, respectively. By exploiting the self-tuning feature of the IC (1), (2), G_T can

be expressed for the linear and saturation ranges of the IC [41]:

$$
G_T = \begin{cases}
\frac{4G_g G_{IC} |Y_{12}|^2}{|(Y_{11}+Y_g)(Y_{22}+G_{IC}+j2\pi f C_{IC}(s_{\min}))-Y_{12}^2|^2} \\
\quad \text{if } B_{\text{out}} \geq -2\pi f C_{IC}(s_{\min}) \\[2ex]
\frac{4G_g G_{IC} |Y_{12}|^2}{|(Y_{11}+Y_g)(Y_{22}+G_{IC}-jB_{\text{out}})-Y_{12}^2|^2} \\
\quad \text{if } -2\pi f C_{IC}(s_{\max}) < B_{\text{out}} < -2\pi f C_{IC}(s_{\min}) \\[2ex]
\frac{4G_g G_{IC} |Y_{12}|^2}{|(Y_{11}+Y_g)(Y_{22}+G_{IC}+j2\pi f C_{IC}(s_{\max}))-Y_{12}^2|^2} \\
\quad \text{if } B_{\text{out}} \leq -2\pi f C_{IC}(s_{\max})
\end{cases}
\tag{4}
$$

where B_{out} is the susceptance of the input admittance $Y_{\text{out}} = G_{\text{out}} + jB_{\text{out}} = Y_{22} - Y_{12}^2/(Y_{11}+Y_g)$ seen from the IC towards the network. Hence, B_{out} corresponds to B_A in (2). It is worth noticing that G_T reduces to the Power Transfer Efficiency (PTE) in case the reader antenna is perfectly matched to 50 Ω [42]. G_T is the indicator that has to be maximized to achieve a reliable communication link.

Denoting with $P_{av,R}$ the maximum output power that the reader is capable to provide (generally 1 W), the power margin M of the link can be defined (in dB) as:

$$
M = G_T + P_{av,R} - P_{\text{chip}} - M_0 \tag{5}
$$

where $M_0 = 3$ dB is an additional safety margin to account for non-controllable parameters of the network. A reliable trans-cutaneous communication link is achieved providing that $M > 0$ dB. By assuming $P_{av,R} = 1$ W then, by (5) the desired gain is constrained to $G_T \geq -40.6$ dB. Hence, G_T will be hereafter the key performance indicator to be optimized for the design of the implanted RFID transponder.

IV. DESIGN AND NUMERICAL ANALYSIS

This section resumes the design of the two modules of the trans-cardiac link. It comprises two steps related to the interrogator antenna and the antennified valve. For a selected configuration, the sensitivity to the possible misalignment between the valve and the external antenna is then evaluated in detail. Finally, the maximum Specific Absorption Rate (SAR) is computed to discuss compliance with safety regulations.

A. Performance of the Interrogating Antenna

The interrogating antenna is first matched to 50 Ω at 900 MHz, in presence of the valve stent but without the harvesting loop. It is aligned with the valve along the sagittal axis (Fig. 7(b)). The length of the stripes (parameter d) is optimized according to the procedure described in [38], here not repeated for brevity. The reflection coefficient S_{11} for the optimal size $d = 2$ mm is shown in Fig. 7(c) and it is well-tuned to 900 MHz, as required.

B. Optimization of the Loop Harvester

The loop harvester is hence optimized, by accounting for the reader antenna as above, by maximizing the Transducer Power
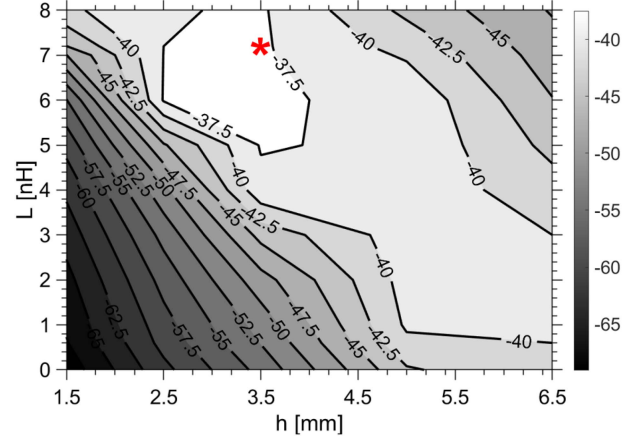

Fig. 8. Isolines of the Transducer Power Gain G_T (in *dB*) at 900 MHz v.s. design parameters of the loop coupler {loop's height, inductor}. The red star represents the selected configuration.
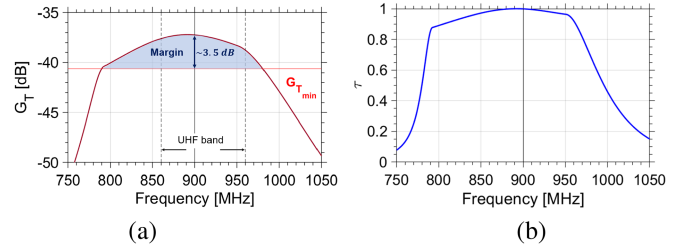

Fig. 9. Simulated (a) Transducer Power Gain G_T and (b) Power Transfer Coefficient (τ) of the selected configuration {$h = 3.5$ mm; $L = 7.2$ nH}. Margin is evaluated for $P_{av,R} = 1$ W.

Gain of the two-port link. Fig. 8 shows the isolines of G_T at 900 MHz by varying the parameters of the loop, namely $1.5 \leq h \leq 6.5$ mm and $0 \leq L \leq 8$ nH. The optimal regions (in white and light grey) are those with $G_T \geq -40$ dB. A large portion of the chart can be exploited, so that multiple configurations are possible. The resulting device will be hence expected to be rather robust against manufacturing imperfections. For instance, by considering the configuration {$h = 3.5$ mm; $L = 7.2$ nH}, the corresponding G_T profile over frequency is shown in Fig. 9(a). Thanks to the self-tuning property of the IC, there is the typical nearly flat profile over broadband and a power margin $M \geq 0$ dB, fully comprising the worldwide RFID-UHF band. Focusing on 900 MHz, the power margin is $M \simeq 3.5$ dB. It is worth computing the power transfer coefficient τ, as in [43], between the antennified valve and the IC, that quantifies the portion of the power collected by the valve that is transferred to the IC. The peak value ($\tau = 0.99$) is centered around 900 MHz, hence the antenna is perfectly matched with the IC (Fig. 9(b)).

C. Tolerance to Misalignment

The degradation of the power margin when the reader antenna is shifted along the longitudinal and latitudinal direction is shown in Fig. 10(a), (b). The communication link appears overall robust to misalignment ($M \geq 0$ dB) up to a displacement of the reader antenna of ± 2 cm (Table II(a),(b)). Instead, the worst-case scenario regards the angular displacement (Fig. 10(c)): the link is
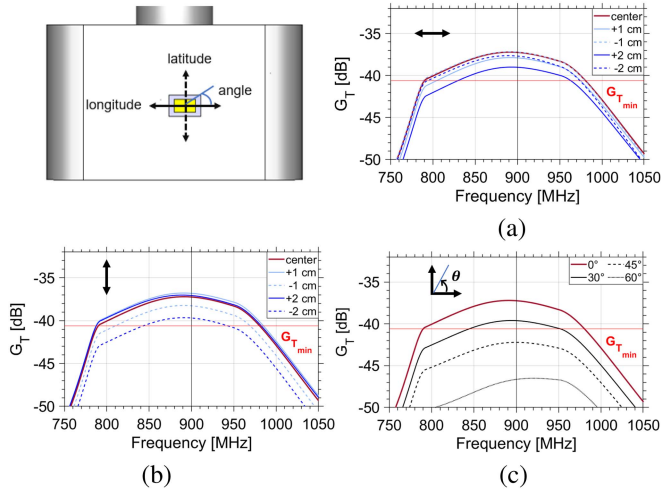
(a)

(b)

(c)

Fig. 10.   Simulated Transducer Power Gain G_T of the optimal configuration in case of: (a) longitudinal, (b) latitudinal, and (c) angular misalignment.

TABLE II
POWER MARGIN [DB] AT 900 MHZ FOR (A) LONGITUDINAL, (B) LATITUDINAL, AND (C) ANGULAR DISPLACEMENT [CM]

$\triangle x$	M	$\triangle y$	M	$\triangle \phi$	M
+1	+2.7	+1	+3.8	0°	+3.4
+2	+1.6	+2	+3.5	30°	+1.0
−1	+3.4	−1	+2.3	45°	−1.6
−2	+2.9	−2	+1.0	60°	−6.0

(a)   (b)   (c)

feasible up to $\triangle\phi = 30°$ (Table II(c)) after that the polarization mismatch between the two antennas becomes detrimental.

D. Specific Absorption Rate Constraint

Regulations on the power delivered by the contacting reader's antenna to the thorax require that the Specific Absorption Rate $SAR = \sigma|E|^2/2\rho$, (where σ and ρ are the local electric conductivity and mass density of the human tissue, and E the peak value of the electric field induced in the body), averaged onto 10 g mass must be $SAR< 2$ W/kg. This imposes a limitation on the emitted power $P_{av,R}$ or on the interrogation rate. Denoting with $D \leq 1$ the duty cycle of the interrogator, the maximum SAR in the body can be related to the duty cycle [44], [45] by the expression $SAR(P_{av,R},D)=SAR_1 \times D$ where SAR_1 corresponds to $P_{av,R} = 1$ W and is shown in Fig. 11. The system is completely compliant with the restrictive electromagnetic exposure limit with a duty cycle $D=SAR_{\max}/SAR_{1,max} = 2/17.6 = 0.11$ (about 3 interrogations per second for sensor-oriented IC [34]) when $P_{av,R} = 1$ W.

V. PROTOTYPE AND EXPERIMENTS

To corroborate the above numerical analysis, this section introduces a mock-up of the antennified-valve prosthesis and the experimental arrangements for the electromagnetic characterization. Some placement depths of the implantation site and tolerance to the misalignment are evaluated.
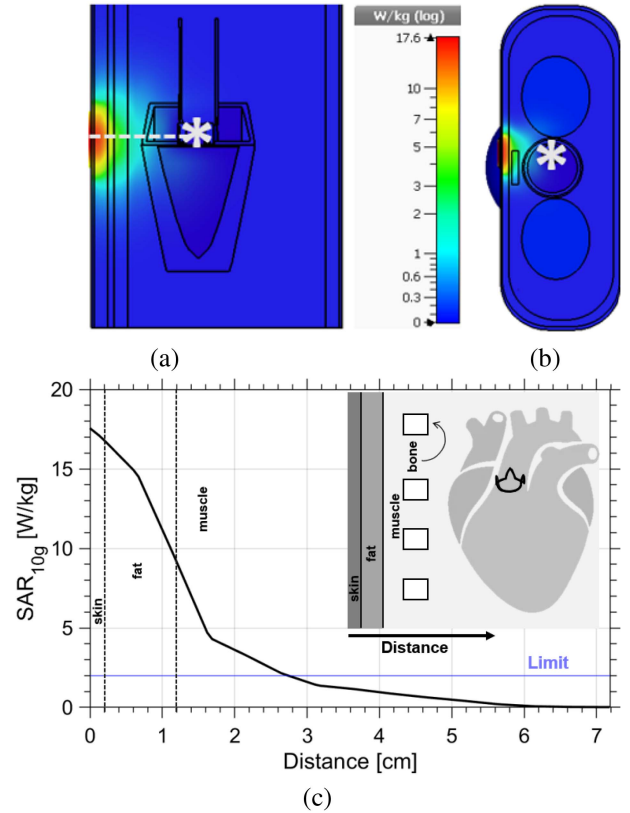

(a)   (b)

(c)

Fig. 11.   Simulated SAR at 900 MHz delivered by the microstrip slot (with unitary duty cycle) inside the layered model of the chest corresponding to $P_{av,R} = 1$ W and averaged onto 10 g. Cross-section over (a) plane yz and (b) plane xz. The white star indicates the position of the valve. (c) 2D plot along the dotted line.
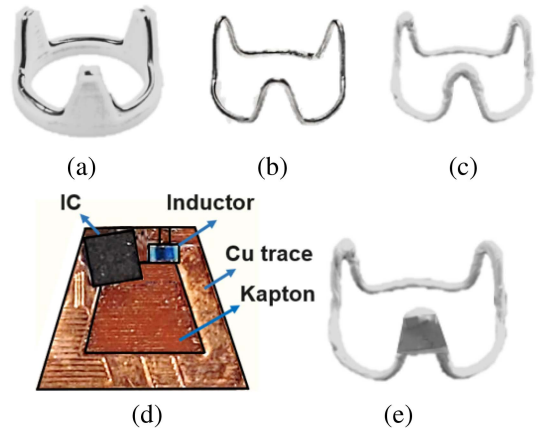

Fig. 12.   Fabrication of the tricusp valve mock-up: (a) wire shaping on a plastic mold, (b) shaped stent, (c) stent coated with a white PTFE film, (d) detail of the loop with IC and inductor, and (e) final valve mock-up with the loop placed in front of a cusp and coated with PTFE.

A. Prototype

A mock-up of the metallic stent of the valve is emulated by a malleable tin wire (wire diameter 1 mm, $\sigma = 8.69 \times 10^6$ S/m) that was shaped with the help of a plastic mold made with a 3D printer (Fig. 12(a)). Then, the wire terminals were soldered to produce a closed loop (Fig. 12(b)). Afterwards, the

Fig. 14. Simulated and measured reflection coefficient of the reader antenna. Results from both the numeric anthropomorphic and homogeneous models are reported.

Fig. 15. Transducer Power Gain G_T vs. frequency: (a) comparison among measurements and simulations of the antennified-valve placed at 7 cm of depth in the liquid mimicking the thorax (the ± 3 dB shadowed region accounts for the manufacturing tolerances); (b) measured G_T when the valve is placed at different depths. Results from both the numeric anthropomorphic and homogeneous models are reported.
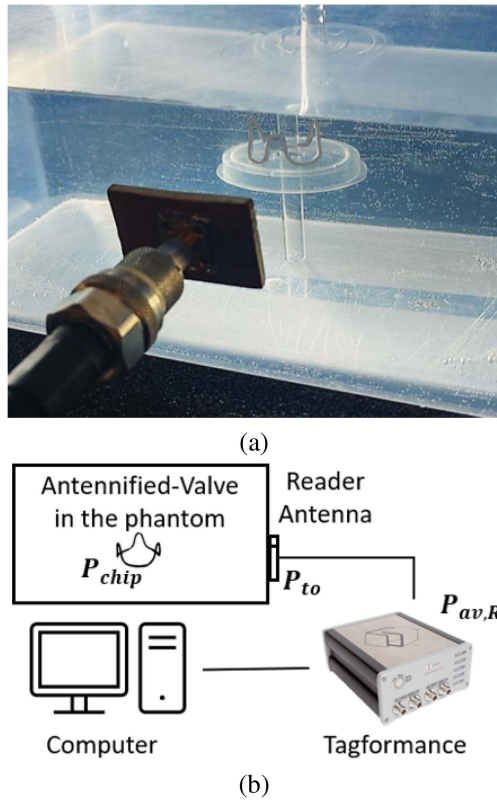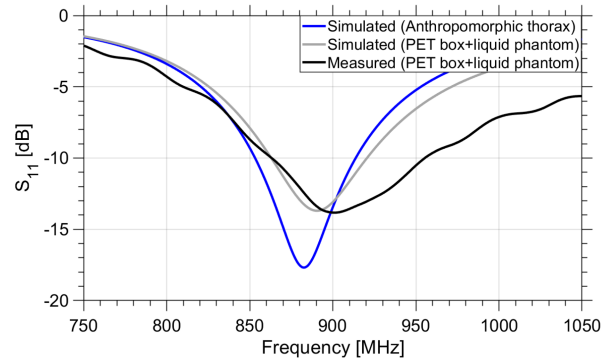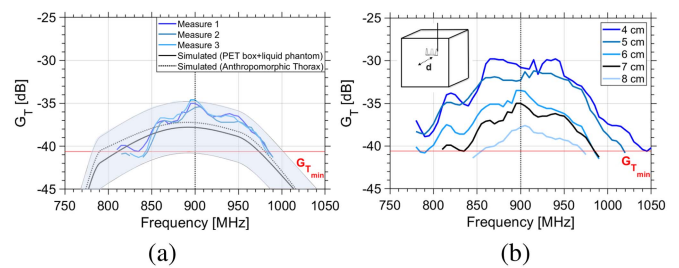

Fig. 13. (a) Experimental setup involving a liquid equivalent of the thorax. (b) Block diagram of the measurement setup.

stent was coated with a PolyTetraFluoroEthylene (PTFE) film ($\varepsilon = 2.1$, $\tan \delta = 0.00001$ [46], thickness 0.2 mm Fig. 12(c)). The loop coupler ($h = 3.5$ mm), instead, was etched with a milling machine on a sheet of flexible Kapton substrate (thickness 0.125 mm), then the IC and inductor ($L = 7.2$ nH) were mounted on the traces by a pick&place machine using a solder paste (conductive epoxy CW2400 by Chemtronics) as shown in Fig. 12(d). Finally, the loop was placed in front of a cusp and fixed by means of the PTFE film (Fig. 12(e)).

B. Electromagnetic Characterization With a Liquid Phantom

The chest is emulated by a PET box ($\varepsilon = 2.1$, $\sigma = 2 \times 10^{-4}$ S/m [47], thickness 2 mm) filled with a liquid phantom ($\varepsilon = 54$, $\sigma = 1.05$ S/m [48]) accounting for the high losses of the interposed human tissues. The antennified-valve was immersed in the fluid as in realistic conditions. The reader antenna was hence attached to the external surface of the container (Fig. 13(a)), without the silicone layer (given the presence of the PET box) at a distance of 7 cm from the device. To corroborate the experimental results, the measurement setup was also replicated in simulation. Despite being a simpler model than the anthropomorphic thorax above, it is nevertheless expected to reproduce the dominant electromagnetic phenomena. Fig. 14 hence shows the simulated and measured reflection coefficient of the reader antenna. Measurement and simulations compare well, and the only remarkable difference between the anthropomorphic model and the homogeneous one is just a

reduction in the null depth, with no relevant frequency shift. The assembled prototype was electromagnetically characterized in the frequency band 750–1050 MHz by connecting the reader antenna to the Voyantic Tagformance station. Starting from a zero value, the input power of the reader antenna was automatically gradually increased until the IC started responding. This threshold power is the turn-on power P_{to}. At this condition, the power collected by the RFID IC equals to its sensitivity P_{chip}, so that by following (3), the Transducer Power Gain is evaluated as $G_T = P_{chip}/P_{to}$ (Fig. 13(b)). Measurements were repeated three times and compared with the simulated outcomes of the corresponding experimental setup. The resulting measured Transducer Power Gain (Fig. 15(a)) is higher than the threshold in the whole UHF-RFID band, as expected, and compares well with the simulations, with a difference of less than 3 dB. Also in this case the difference between the two body models is negligible and therefore the homogeneous one is adequate for the experimental test. The oscillations are due to the self-tuning feature of the IC that automatically adjusts its internal capacitance to keep the antenna-IC matching stable over frequency [41].

In a second measurement, the valve mock-up was placed at some distances $4 < d < 9$ cm from the surface of the box to emulate possible anatomical variability of the chest's size as well as of the thoracic organs. Fig. 15(b) shows a widening of the G_T profile as well as an improved power margin when the depth
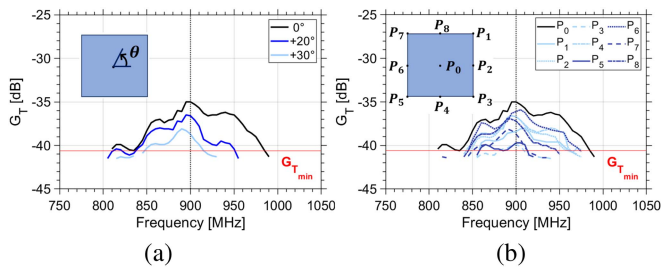
Fig. 16. Measured Transducer Power Gain G_T when the reader antenna (a) is rotated in the center position and (b) is placed at different points over a square grid 2×2 cm^2.

of the implant decreases. These measurements demonstrate the feasibility of communication up to 8 cm skin-valve distance.

C. Read Area

In a third experiment, some mutual displacements between the two antennas are replicated, as in Fig. 16, namely rotations and shifts. The distance of the valve from the interrogating on-body slot antenna was fixed at 7 cm. Fig. 16(a) shows the G_T when the reader antenna was incrementally rotated counterclockwise while remaining perfectly aligned with the valve (central position). A power margin of at least $\simeq 2$ dB is achieved with a rotation up to $+30°$ at 900 MHz as found numerically in Section IV. Finally, the slot antenna was moved along a 9-points grid (Fig. 16(b)). The system looks resilient for displacements up to 2 cm from the axial (central) position, as expected.

VI. CONCLUSIONS AND FUTURE WORKS

The paper has demonstrated that the metallic stent of an aortic valve prosthesis can be used as a *structural* UHF loop antenna to add communication capabilities to the device itself. By means of a properly designed add-on, in the form of a conformable thin trapezoidal coupler loop, placed in close proximity to one cusp, and embedded in the same dielectric coating, the electromagnetic field coming from an external reader can be collected by the stent to power up a sensor-oriented RFID IC. A sufficient power margin (up to 3 dB) in the link budget is obtained notwithstanding potential user-specific placement as well as misalignment between the antennas.

Future activity will focus on further experimental corroboration with a more realistic phantom up to an in-vivo test on animals. While this paper only addressed the communication issues, research effort must be still devoted to the sensor topic, namely the integration of specific probes into the coupler for the monitoring of deformation [47] and, above all, of pressure gradients [14]. Finally, as the valve stent is generally equipped with three cusps, up to three sensing points could be envisaged thus enabling redundancy and multi-parametric sensing.

REFERENCES

[1] S. L. Murphy et al., "Mortality in the United States, 2017. NCHS data brief, no 328," 2018, pp. 1–8.

[2] E. Marcelli, B. Bortolani, I. Corazza, and L. Cercenelli, "A novel sensorized heart valve prosthesis: Preliminary in vitro evaluation," *Sensors*, vol. 18, no. 11, 2018, Art. no. 3905.

[3] B. Vennemann, D. Obrist, and T. Rösgen, "A smartphone-enabled wireless and batteryless implantable blood flow sensor for remote monitoring of prosthetic heart valve function," *PLoS One*, vol. 15, no. 1, 2020, Art. no. e0227372.

[4] A. B. Goldstone et al., "Mechanical or biologic prostheses for aortic-valve and mitral-valve replacement," *New England J. Med.*, vol. 377, no. 19, pp. 1847–1857, 2017.

[5] D. Capodanno et al., "Standardized definitions of structural deterioration and valve failure in assessing long-term durability of transcatheter and surgical aortic bioprosthetic valves: A consensus statement from the European association of percutaneous cardiovascular interventions (EAPCI) endorsed by the European society of cardiology (ESC) and the European association for cardio-thoracic surgery (EACTS)," *Eur. Heart J.*, vol. 38, no. 45, pp. 3382–3390, 2017.

[6] E. G. Butchart et al., "Recommendations for the management of patients after heart valve surgery," *Eur. Heart J.*, vol. 26, no. 22, pp. 2463–2471, 2005.

[7] P. Lancellotti et al., "Recommendations for the imaging assessment of prosthetic heart valves: A report from the European association of cardiovascular imaging endorsed by the chinese society of echocardiography, the inter-american society of echocardiography, and the brazilian department of cardiovascular imaging," *Eur. Heart J. - Cardiovasc. Imag.*, vol. 17, no. 6, pp. 589–590, 2016. [Online]. Available: https://doi.org/10.1093/ehjci/jew025

[8] A. Kiourti, "RFID antennas for body-area applications: From wearables to implants," *IEEE Antennas Propag. Mag.*, vol. 60, no. 5, pp. 14–25, Oct. 2018.

[9] D. Rodrigues, A. I. Barbosa, R. Rebelo, I. K. Kwon, R. L. Reis, and V. M. Correlo, "Skin-integrated wearable systems and implantable biosensors: A comprehensive review," *Biosensors*, vol. 10, no. 7, 2020, Art. no. 79.

[10] Z. Liu, N. Meyendorf, and N. Mrad, "The role of data fusion in predictive maintenance using digital twin," in *AIP Conf. Proc.*, vol. 1949, no. 1. AIP Publishing LLC, 2018, Art. no. 020023.

[11] M. Rav Acha, E. Soifer, and T. Hasin, "Cardiac implantable electronic miniaturized and micro devices," *Micromachines*, vol. 11, no. 10, 2020, Art. no. 902.

[12] W. T. Abraham and L. Perl, "Implantable hemodynamic monitoring for heart failure patients," *J. Amer. College Cardiol.*, vol. 70, no. 3, pp. 389–398, 2017.

[13] A. Joury et al., "Leadless and wireless cardiac devices: The next frontier in remote patient monitoring," *Curr. Problems Cardiol.*, vol. 46, no. 5, 2021, Art. no. 100800.

[14] Y. X. Ang, A. Z. M. Khudzari, and M. S. M. Ali, "Non-invasive treatment for coronary in-stent restenosis via wireless revascularization with nitinol active stent," *IEEE Trans. Biomed. Eng.*, vol. 68, no. 12, pp. 3681–3689, Dec. 2021.

[15] K. B. Chandran, S. E. Rittgers, and A. P. Yoganathan, *Biofluid Mechanics: The Human Circulation*. Boca Raton, FL, USA: CRC Press, 2006.

[16] G. Marrocco and L. Mattioni, "Naval structural antenna systems for broadband HF communications," *IEEE Trans. Antennas Propag.*, vol. 54, no. 4, pp. 1065–1073, Apr. 2006.

[17] S. A. A. Shah, Y.-H. Lim, and H. Yoo, "A novel development of endovascular aortic stent system featuring promising antenna characteristics," *IEEE Trans. Antennas Propag.*, vol. 70, no. 3, pp. 2214–2222, Mar. 2022.

[18] C. Occhiuzzi, G. Contri, and G. Marrocco, "Design of implanted RFID tags for passive sensing of human body: The STENTag," *IEEE Trans. Antennas Propag.*, vol. 60, no. 7, pp. 3146–3154, Jul. 2012.

[19] M. Alghrairi, N. Sulaiman, W. Z. W. Hasan, H. Jaafar, and S. Mutashar, "Design a wireless pressure sensor with an ellipse and a circular shape to monitor the pressure within the coronary artery," *IEEE Access*, vol. 10, pp. 92158–92165, 2022.

[20] P. Avaltroni, S. Nappi, and G. Marrocco, "Antennifying orthopedic bone-plate fixtures for the wireless monitoring of local deep infections," *IEEE Sensors J.*, vol. 21, no. 18, pp. 21012–21021, Sep. 2021.

[21] N. Panunzio et al., "Cyber-tooth: Antennified dental implant for RFID wireless temperature monitoring," in *Proc. IEEE Int. Conf. RFID Technol. Appl.*, 2021, pp. 211–214.

[22] M. Gagliardi, C. Occhiuzzi, R. Verzicco, and G. Marrocco, "How to transform an aortic valve prostheses into an UHF antenna for the RFID-based wireless monitoring of the cardiac health," in *Proc. 16th Eur. Conf. Antennas Propag.*, 2022, pp. 1–5.

[23] Meril, Accessed: May. 2, 2022. [Online]. Available: https://www.merillife.com/medical-devices/vascular-intervention/heart-valves/dafodil-pericardial-bioprosthesis

[24] P. Bloomfield, "Choice of heart valve prosthesis," *Heart*, vol. 87, no. 6, pp. 583–589, 2002.

[25] P. Blanke et al., "Computed tomography assessment for transcatheter aortic valve in valve implantation: The vancouver approach to predict anatomical risk for coronary obstruction and other considerations," *J. Cardiovasc. Comput. Tomogr.*, vol. 10, no. 6, pp. 491–499, 2016.

[26] J. Lesnikowski, "Dielectric permittivity measurement methods of textile substrate of textile transmission lines," *Przeglad Elektrotechniczny*, vol. 88, no. 3A, pp. 148–151, 2012.

[27] IFAC-CNR, "Calculation of the dielectric properties of body tissues in the frequency range 10 Hz - 100 GHz," available on line. Accessed: Nov. 1, 2021. [Online]. Available: http://niremf.ifac.cnr.it/

[28] C. Occhiuzzi, S. Parrella, F. Camera, S. Nappi, and G. Marrocco, "RFID-based dual-chip epidermal sensing platform for human skin monitoring," *IEEE Sensors J.*, vol. 21, no. 4, pp. 5359–5367, Feb. 2021.

[29] Dupont, "Kapton," Accessed: May 2022. [Online]. Available: https://www.dupont.com/products/kapton-hn.html

[30] K. Li et al., "A generic soft encapsulation strategy for stretchable electronics," *Adv. Funct. Mater.*, vol. 29, no. 8, 2019, Art. no. 1806630.

[31] F. Gao, Z. Guo, M. Sakamoto, and T. Matsuzawa, "Fluid-structure interaction within a layered aortic arch model," *J. Biol. Phys.*, vol. 32, no. 5, pp. 435–454, 2006.

[32] N. Yogeswaran et al., "New materials and advances in making electronic skin for interactive robots," *Adv. Robot.*, vol. 29, no. 21, pp. 1359–1373, 2015.

[33] Y.-S. Kim et al., "Scalable manufacturing of solderable and stretchable physiologic sensing systems," *Adv. Mater.*, vol. 29, no. 39, 2017, Art. no. 1701312.

[34] Axzon, "Magnus-S3 passive sensor IC," Accessed: Dec. 7, 2021. [Online]. Available: https://axzon.com/rfm3300-d-magnus-s3-m3d-passive-sensor-ic/

[35] F. Nanni, S. Nappi, and G. Marrocco, "Potentiometric sensing by means of self-tuning RFID ICs," in *Proc. IEEE Int. Conf. RFID*, 2022, pp. 17–22.

[36] I. Ullah, B. Sanz-Izquierdo, and J. C. Batchelor, "Dual RFID tag system for AC current sensing," in *Proc. 16th Eur. Conf. Antennas Propag.*, 2022, pp. 1–5.

[37] F. Naccarata, G. M. Bianco, and G. Marrocco, "Sensing performance of multi-channel RFID-based finger augmentation devices for tactile internet," *IEEE J. Radio Freq. Identif.*, vol. 6, pp. 209–217, 2022.

[38] C. Miozzi, G. Saggio, E. Gruppioni, and G. Marrocco, "Constrained safety-integrity performance of through-the-arms UHF-RFID transcutaneous wireless communication for the control of prostheses," *IEEE J. Radio Freq. Identif.*, vol. 3, no. 4, pp. 236–244, Dec. 2019.

[39] C. Miozzi, F. Amato, and G. Marrocco, "Performance and durability of thread antennas as stretchable epidermal UHF RFID tags," *IEEE J. Radio Freq. Identif.*, vol. 4, no. 4, pp. 398–405, Dec. 2020.

[40] S. J. Orfanidis, "Electromagnetic waves and antennas," Accessed: Aug. 3, 2022. [Online]. Available: http://eceweb1.rutgers.edu/orfanidi/ewa/

[41] G. M. Bianco, S. Amendola, and G. Marrocco, "Near-field constrained design for self-tuning UHF-RFID antennas," *IEEE Trans. Antennas Propag.*, vol. 68, no. 10, pp. 6906–6911, Oct. 2020.

[42] P. Jayathurathnage, M. Vilathgamuwa, and C. Simovski, "Revisiting two-port network analysis for wireless power transfer (WPT) systems," in *Proc. IEEE 4th Southern Power Electron. Conf.*, 2018, pp. 1–5.

[43] G. M. Bianco and G. Marrocco, "Fingertip self-tuning RFID antennas for the discrimination of dielectric objects," in *Proc. 13th Eur. Conf. Antennas Propag.*, 2019, pp. 1–4.

[44] M. A. Akram, K.-W. Yang, and S. Ha, "Duty-cycled wireless power transmission for millimeter-sized biomedical implants," *Electronics, vol.* 9, no. 12, pp. 1–15, 2020. [Online]. Available: https://www.mdpi.com/2079-9292/9/12/2130

[45] C. Occhiuzzi, C. Vallese, S. Amendola, S. Manzari, and G. Marrocco, "Night-care: A passive RFID system for remote monitoring and control of overnight living environment," *Procedia Comput. Sci.*, vol. 32, pp. 190–197, 2014.

[46] Q. Qiao, L. Zhang, F. Yang, Z. Yue, and A. Z. Elsherbeni, "A high sensitivity capacitively-loaded UHF RFID temperature sensor tag using PTFE material," in *Proc. IEEE Antennas Propag. Soc. Int. Symp.*, 2014, pp. 1310–1311.

[47] S. Nappi, L. Gargale, F. Naccarata, P. P. Valentini, and G. Marrocco, "A fractal-RFID based sensing tattoo for the early detection of cracks in implanted metal prostheses," *IEEE J. Electromagn., RF, Microw. Med. Biol.*, vol. 6, no. 1, pp. 29–40, Mar. 2021.

[48] Speag Swiss, "Body tissue simulating liquids," Accessed: Jun. 15, 2022. [Online]. Available: https://speag.swiss/components/materials-liquids/msl/